

# Microstructure/geometric imperfection sensitivity on the thermo-mechanical nonlinear stability behavior of functionally graded plates using four variable refined structural kinematics

*J Strain Analysis*

1–17

© IMechE 2020

Article reuse guidelines:

sagepub.com/journals-permissions

DOI: 10.1177/0309324720972874

journals.sagepub.com/home/sdj



Mohit Rajput and Ankit Gupta

## Abstract

The present work deals with the nonlinear stability characteristics of geometrically imperfect shear deformable functionally graded plates (FGP) subjected to thermo-mechanical loads. The equilibrium, stability, and compatibility equations are derived using trigonometric shear-strain function based refined shear deformation plate theory. The displacement field used in the present study has been employed for FGP for the first time. The in-plane and transverse displacements consist of bending and shear components, whereas the displacement field contains only four unknowns. Geometric nonlinearity has been incorporated in the formulation in a von-Karman sense. A generalized porosity model has also been developed to accommodate both even and uneven porosity distribution reported in the literature. Various models of geometric imperfection have been modeled using imperfection function. An exact expression for the critical buckling load and critical buckling thermal load of geometrically imperfect porous FGPs for various loading conditions have been developed. After ensuring the excellent accuracy of the developed expression, the influence of geometric imperfection, porosity inclusion, and geometric configuration on the nonlinear stability of FGPs has been discussed extensively. The results presented in this paper will be used as a benchmark for future research.

## Keywords

Functionally graded plates, buckling response, thermal response, exact solution, geometric nonlinearity, geometric imperfection, porosity

Date received: 2 July 2020; accepted: 15 October 2020

## Introduction

The idea of functionally graded materials (FGMs) was first considered in Japan in 1984 during a space-plane project by the material scientists.<sup>1</sup> These advanced heterogeneous composite materials possess the continuous gradation of mechanical properties in the preferred direction. This is obtained by changing the volume fraction of the constituent materials. FGMs have already proven its potential as structural elements in extreme working environments. FGMs are made from the homogeneous composition of metal and ceramic. With the increasing use of these materials for structural elements in several engineering applications, it needs to analyze the structural characteristics of FGMs plates.<sup>2–5</sup>

Although there are several reports available on the stability of functionally graded plate (FGPs), the articles on nonlinear stability of porous FGPs with

geometric imperfection subjected to the thermo-mechanical environment are limited in number. Shariat et al.<sup>6</sup> studied the buckling response of geometrically imperfect functionally graded plate (FGP) using classical plate theory (CPT). Lanhe<sup>7</sup> derived the equilibrium and stability equations for a simply-supported rectangular FGP subjected to thermal loads using first-order shear deformation theory (FSDT). Javaheri and Eslami<sup>8</sup> employed CPT to developed the equilibrium and stability equations using a variational approach for the perfect FGP. Gupta and Talha<sup>9,10</sup> investigated the

School of Engineering, Shiv Nadar University, Uttar Pradesh, India

### Corresponding author:

Ankit Gupta, School of Engineering, Shiv Nadar University, Gautam Buddha Nagar, Uttar Pradesh 201314, India.

Email: Ankit.gupta1@snu.edu.in

influence of geometric imperfection and porosity on the post-buckling behavior of FGP using hybrid higher-order shear deformation theory (HSDT). A new method has been presented by Mohammadi et al.<sup>11</sup> for decoupling the stability equation of moderately thick FGP based on a single Sin-series solution (Levy's method). Zhang et al.<sup>12</sup> presented the critical buckling and dynamic post-buckling behavior of imperfect annular FGPs using the nonlinear plate theory.

The exact solution using higher-order shear deformation theory (HSDT) for the buckling response of the composite plate has been investigated by Fazzolari et al.<sup>13</sup> Thai and Choi<sup>14</sup> presented the closed-form solution for the buckling analysis of functionally graded plate using two variable refined plate theory. Shariat and Eslami<sup>15,16</sup> presented the rectangular FGP with geometric defects for perfect and imperfect plate subjected to thermal and mechanical loading based on polynomial higher-order shear theory (TSDT). The large-amplitude vibration and the post-buckling response of FGPs with geometric imperfection and microstructure defects have been studied by Gupta and Talha.<sup>17</sup> Shariat and Eslami<sup>18</sup> represented the buckling analysis of perfect FGP under in-plane compressive loading using FSdT. The buckling analysis of circular FGP made of porous material was presented by Mojahedin et al.<sup>19</sup> based on HSDT. A four-variable refined plate theory was established by Bouiadjra et al.<sup>20</sup> for the buckling analysis of FGP. Alijani and Amabili<sup>21</sup> used a multi-degree of freedom energy approach to study the stability response of geometrically nonlinear FGM plate in thermal environments. Yanga and Shen<sup>22</sup> explored the post-buckling behavior of gradient plates using a semi-analytical approach. Dinh and Van Tung<sup>23</sup> employed HSDT with the conjunction of von Karman nonlinearity to explore the post-buckling response of FGP under thermo-mechanical loads.

Li et al.<sup>24</sup> introduced the non-linear thermo-mechanical post-buckling analysis of circular FGP with geometric imperfection subjected to mechanical and thermal loading. The thermal buckling analysis of FGP with geometrically imperfect plate was investigated by Shariat and Eslami<sup>25,26</sup> subjected to thermal loading based on CPT and FSdT. Liew et al.<sup>27</sup> studied the post-buckling response of piezoelectric FGP subjected to thermo-electro-mechanical loading. The buckling response of FGPs under uniaxial compression, biaxial compression, and combined compression and tension was studied by Sherafat and Ovesy.<sup>28</sup> Morimoto and Tanigawa<sup>29</sup> presented the buckling behavior of orthotropic inhomogeneous rectangular plates under uniform in-plane compression. Abrate<sup>30</sup> obtained the free vibration, buckling, and static deflection of FGP. The buckling behavior of thick FGP has been studied by Bodaghi and Saidi<sup>31</sup> based on HSDT using Levy's method. Park and Kim<sup>32</sup> examined the post-buckling response of FGM plate under the thermal environment. Uymaz and Aydogdu<sup>33</sup> employed the linear

strain energy concept and Ritz method to examine the buckling characteristics of graded plates under mechanical loads. Liew et al.<sup>27</sup> used a Galerkin-differential quadrature iteration based scheme with third-order deformation theory to study the post-buckling response of the piezoelectric graded plate.

In the view of the above discussion, it is noticed that very few reports are available which deals with the nonlinear thermo-mechanical buckling response of geometrically imperfect porous FGP. Therefore, the present study aims to drive an exact expression for the critical buckling load and buckling temperature of geometrically imperfect porous FGP with a von-Karman sense of geometric nonlinearity. A generic function has also been developed to account for both even and uneven porosity distribution in FGP. The equilibrium, stability, and compatibility equations for the rectangular imperfect porous FGP have been derived based on four variable refined plate theory. The trigonometric shear-strain function has been used in the present article for the first time for FGP. The same function was first given by Suganyadevi and Singh<sup>34</sup> for laminated composite plates. The effect of geometric imperfection, geometric configuration, gradation rules, and porosity including on the nonlinear buckling behavior of FGP has been studied in detail.

## Geometric configuration and effective materials properties of FGP

The geometric configuration of the FGP with dimensions ( $a \times b \times h$ ) in the Cartesian coordinate system is shown in Figure 1. A new mathematical model has been developed to accommodate the porosity distribution in the plate as given in equation (1). A specific attribute of the present model is that it includes both even and uneven distribution of porosity reported in the literature.<sup>35</sup>

$$\begin{aligned} E(z) &= E_m + E_{cm} \left( \frac{z}{h} + \frac{1}{2} \right)^k \\ &\quad - (E_m + E_c) \tan^{-1} \left( \frac{\lambda}{2} \right) \left( 1 - 2B \frac{|z|}{h} \right) \\ \alpha_T(z) &= \alpha_m + \alpha_{cm} \left( \frac{z}{h} + \frac{1}{2} \right)^k \\ &\quad - (\alpha_m + \alpha_c) \tan^{-1} \left( \frac{\lambda}{2} \right) \left( 1 - 2B \frac{|z|}{h} \right) \end{aligned} \quad (1)$$

where

$$\begin{aligned} E_{cm} &= E_c - E_m \\ \alpha_{cm} &= \alpha_c - \alpha_m \end{aligned} \quad (2)$$

where " $\lambda$ " indicates the porosity volume fraction which ranges from 0 to 1. If  $\lambda = 0$ , it represents that the plate is nonporous whereas as the value of  $\lambda$  increases, porosity in the plate increases. Whereas B ( $0 < B < 1$ ) is porosity distribution factor. When  $B = 0$  and  $B = 1$

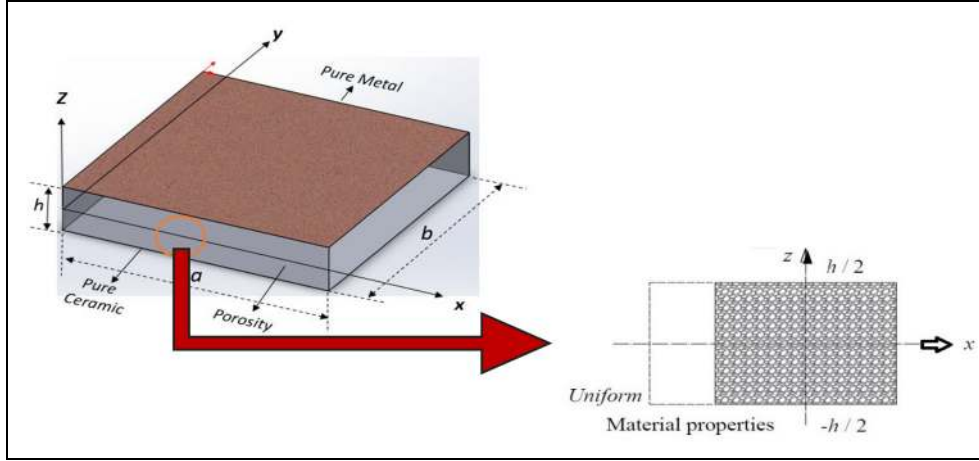


**Figure 1.** Geometric configuration of porous FGP.

present the even and uneven porosity distribution respectively. “ $z$ ” is the thickness coordinate variable,  $h$  is the thickness of the plate, and  $k$  is the power-law index. We assume that the modulus of elasticity  $E(z)$  and the coefficient of thermal expansion  $\alpha_T(z)$  vary in the thickness direction “ $z$ .” The ceramic part has high-temperature resistance and the metal part inhibits the fracture under thermal loadings.

### Equilibrium, stability, and governing equations for buckling analysis

The FGP under the various combination of in-plane compressive edge loads  $\delta_x$  and  $\delta_y$ , uniformly distributed along the edge  $x = 0$ ,  $a$  and  $y = 0$ ,  $b$ , respectively, is shown in Figure 2.

#### Structural kinematics

In the present paper, new structural kinematics has been introduced for FGPs. The shear-strain function is based on trigonometric function, which was initially given by Suganyadevi and Singh.<sup>34</sup>

$$\begin{aligned} u(x, y, z) &= u_0(x, y) - z \frac{\partial w_b}{\partial x}(x, y) + f(z) \frac{\partial w_s}{\partial x}(x, y) \\ v(x, y, z) &= v_0(x, y) - z \frac{\partial w_b}{\partial y}(x, y) + f(z) \frac{\partial w_s}{\partial y}(x, y) \\ w(x, y, z) &= w_b(x, y) + w_s(x, y) \end{aligned} \quad (3)$$

where

$$f(z) = \sin(2.5z/h) \cos(2.5z/h) - (2.5z/h) \cos(2.5)$$

Here,  $u$  and  $v$  are the mid-plane displacements of the plate in the  $x$ - and  $y$ -direction, respectively whereas,  $w_b$  and  $w_s$  are the bending and shear components of transverse displacement, respectively. The von-Karman sense of geometric nonlinearity has been incorporated in the strain-displacement relations for non-linear behavior as given below.<sup>15,16</sup>

$$\left. \begin{aligned} \left. \begin{aligned} \varepsilon_{xx} \\ \varepsilon_{yy} \\ \gamma_{xy} \end{aligned} \right\} &= \left. \begin{aligned} \frac{du}{dx} + \frac{1}{2} \left( \frac{dw}{dx} \right)^2 \\ \frac{dv}{dy} + \frac{1}{2} \left( \frac{dw}{dy} \right)^2 \\ \frac{du}{dy} + \frac{dv}{dx} + \left( \frac{dw}{dy} \right) \left( \frac{dw}{dx} \right) \end{aligned} \right\}, \\ \left. \begin{aligned} \gamma_{yz} \\ \gamma_{xz} \end{aligned} \right\} &= \left. \begin{aligned} \frac{dw}{dy} + \frac{dv}{dz} \\ \frac{dw}{dx} + \frac{du}{dz} \end{aligned} \right\} \end{aligned} \quad (4)$$

Using equations (3) and (4)

$$\left. \begin{aligned} \left. \begin{aligned} \varepsilon_{xx} \\ \varepsilon_{yy} \\ \gamma_{xy} \end{aligned} \right\} &= \left. \begin{aligned} \varepsilon_{xx}^0 \\ \varepsilon_{yy}^0 \\ \gamma_{xy}^0 \end{aligned} \right\} + z \left. \begin{aligned} K_{xx}^b \\ K_{yy}^b \\ K_{xy}^b \end{aligned} \right\} + L \left. \begin{aligned} K_{xx}^s \\ K_{yy}^s \\ K_{xy}^s \end{aligned} \right\}, \\ \left. \begin{aligned} \gamma_{yz} \\ \gamma_{xz} \end{aligned} \right\} &= g(z) \left. \begin{aligned} \gamma_{yz}^s \\ \gamma_{xz}^s \end{aligned} \right\} \end{aligned} \quad (5)$$

where

$$\left. \begin{aligned} \left. \begin{aligned} \varepsilon_{xx}^0 \\ \varepsilon_{yy}^0 \\ \gamma_{xy}^0 \end{aligned} \right\} &= \left. \begin{aligned} \frac{du_0}{dx} + \frac{1}{2} \left( \frac{dw_0}{dx} \right)^2 \\ \frac{dv_0}{dy} + \frac{1}{2} \left( \frac{dw_0}{dy} \right)^2 \\ \frac{du_0}{dy} + \frac{dv_0}{dx} + \left( \frac{dw_0}{dy} \right) \left( \frac{dw_0}{dx} \right) \end{aligned} \right\}, \\ \left. \begin{aligned} K_{xx}^b \\ K_{yy}^b \\ K_{xy}^b \end{aligned} \right\} &= - \left. \begin{aligned} \frac{d^2 w_b}{dx^2} \\ \frac{d^2 w_b}{dy^2} \\ \frac{d^2 w_b}{dxdy} \end{aligned} \right\}, \quad \left. \begin{aligned} K_{xx}^s \\ K_{yy}^s \\ K_{xy}^s \end{aligned} \right\} \\ &= - \left. \begin{aligned} \frac{d^2 w_s}{dx^2} \\ \frac{d^2 w_s}{dy^2} \\ \frac{d^2 w_s}{dxdy} \end{aligned} \right\}, \quad \left. \begin{aligned} \gamma_{yz}^s \\ \gamma_{xz}^s \end{aligned} \right\} = \left. \begin{aligned} \frac{dw_s}{dy} \\ \frac{dw_s}{dx} \end{aligned} \right\} \end{aligned} \quad (6a)$$

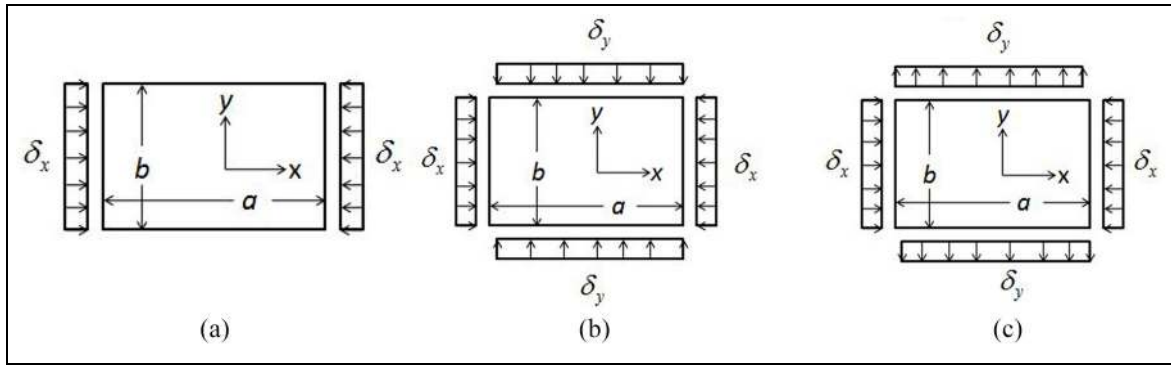


**Figure 2.** The loading conditions of rectangular functionally graded plate: (a) uniaxial compression along x-axis, (b) biaxial compression, and (c) compression in x direction and tension in y direction.

$$L = -f(z), \quad g(z) = 1 + f'(z) \tag{6b}$$

The generalized Hook's law for FGM plate is defined as<sup>20</sup>

$$\begin{Bmatrix} \sigma_{xx} \\ \sigma_{yy} \\ \tau_{xy} \\ \tau_{yz} \\ \tau_{xz} \end{Bmatrix} = \frac{E(z)}{(1-\nu^2)} \begin{bmatrix} 1 & \nu & 0 & 0 & 0 \\ \nu & 1 & 0 & 0 & 0 \\ 0 & 0 & \frac{1-\nu}{2} & 0 & 0 \\ 0 & 0 & 0 & \frac{1-\nu}{2} & 0 \\ 0 & 0 & 0 & 0 & \frac{1-\nu}{2} \end{bmatrix} \begin{Bmatrix} \epsilon_{xx} - \alpha_T(z)\Delta T \\ \epsilon_{yy} - \alpha_T(z)\Delta T \\ \gamma_{xy} \\ \gamma_{yz} \\ \gamma_{xz} \end{Bmatrix} \tag{7}$$

The forces and moments per unit length of the plate expressed in term of the stress component through the thickness are<sup>20</sup>

$$\begin{bmatrix} N_{xx} & M_{xx}^b & M_{xx}^s \\ N_{yy} & M_{yy}^b & M_{yy}^s \\ N_{xy} & M_{xy}^b & M_{xy}^s \end{bmatrix} = \int_{-h/2}^{h/2} \begin{Bmatrix} \bar{\sigma}_{xx} \\ \bar{\sigma}_{yy} \\ \bar{\tau}_{xy} \end{Bmatrix} [1 \quad z \quad L] dz \tag{8}$$

$$\begin{bmatrix} Q_{xz}^s \\ Q_{yz}^s \end{bmatrix} = g(z) \int_{-h/2}^{h/2} \begin{Bmatrix} \bar{\tau}_{xz} \\ \bar{\tau}_{yz} \end{Bmatrix} [1] dz \tag{9}$$

Substituting equations (1), (5), and (7) into equations (8) and (9), gives the constitutive relations as

$$N_{xx} = \frac{E_1}{1-\nu^2} (\epsilon_{xx}^0 + \nu \epsilon_{yy}^0) + \frac{E_2}{1-\nu^2} (k_{xx}^b + \nu k_y^b) + I_1 (k_{xx}^s + \nu k_{yy}^s) - \frac{(1+\nu)}{(1-\nu^2)} (\phi_1)$$

$$N_{yy} = \frac{E_1}{1-\nu^2} (\epsilon_{yy}^0 + \nu \epsilon_{xx}^0) + \frac{E_2}{1-\nu^2} (k_{yy}^b + \nu k_{xx}^b) + I_1 (k_{yy}^s + \nu k_{xx}^s) - \frac{(1+\nu)}{(1-\nu^2)} (\phi_1)$$

$$N_{xy} = \frac{E_1}{2(1+\nu)} \gamma_{xy}^0 + \frac{E_2}{(1+\nu)} k_{xy}^b + \frac{I_1}{(1+\nu)} k_{xy}^s \tag{10a}$$

$$M_{xx}^b = \frac{E_2}{1-\nu^2} (\epsilon_{xx}^0 + \nu \epsilon_{yy}^0) + \frac{E_3}{1-\nu^2} (k_{xx}^b + \nu k_y^b) + I_2 (k_{xx}^s + \nu k_{yy}^s) - \frac{(1+\nu)}{(1-\nu^2)} (\phi_2)$$

$$M_{yy}^b = \frac{E_2}{1-\nu^2} (\epsilon_{yy}^0 + \nu \epsilon_{xx}^0) + \frac{E_3}{1-\nu^2} (k_{yy}^b + \nu k_{xx}^b) + I_2 (k_{yy}^s + \nu k_{xx}^s) - \frac{(1+\nu)}{(1-\nu^2)} (\phi_2)$$

$$M_{xy}^b = \frac{E_2}{2(1+\nu)} \gamma_{xy}^0 + \frac{E_3}{(1+\nu)} k_{xy}^b + \frac{I_2}{(1+\nu)} k_{xy}^s \tag{10b}$$

$$M_{xx}^s = \frac{I_1}{1-\nu^2} (\epsilon_{xx}^0 + \nu \epsilon_{yy}^0) + \frac{I_2}{1-\nu^2} (k_{xx}^b + \nu k_y^b) + I_3 (k_{xx}^s + \nu k_{yy}^s) - \frac{(1+\nu)}{(1-\nu^2)} (\phi_3)$$

$$M_{yy}^s = \frac{I_1}{1-\nu^2} (\epsilon_{yy}^0 + \nu \epsilon_{xx}^0) + \frac{I_2}{1-\nu^2} (k_{yy}^b + \nu k_{xx}^b) + I_3 (k_{yy}^s + \nu k_{xx}^s) - \frac{(1+\nu)}{(1-\nu^2)} (\phi_3)$$

$$M_{xy}^s = \frac{I_1}{2(1+\nu)} \gamma_{xy}^0 + \frac{I_2}{(1+\nu)} k_{xy}^b + \frac{I_3}{(1+\nu)} k_{xy}^s$$

$$Q_{xz}^s = \frac{\gamma_{xz}^s}{2(1+\nu)} I_4$$

$$Q_{yz}^s = \frac{\gamma_{yz}^s}{2(1+\nu)} I_4 \tag{10c}$$

where

$$[\phi_1 \ \phi_2 \ \phi_3] = \int_{-h/2}^{h/2} E(z)\alpha_T(z)[1 \ z \ L] \Delta T(x, y, z) dz \quad (11)$$

From the principle of virtual displacement, the governing equations obtained as<sup>20</sup>

$$\begin{aligned} N_{xx,x} + N_{xy,y} &= 0 \\ N_{yy,y} + N_{xy,x} &= 0 \\ M_{xx,xx}^b + M_{yy,yy}^b + 2M_{xy,xy}^b + N(w) &= 0 \\ M_{xx,xx}^s + M_{yy,yy}^s + 2M_{xy,xy}^s + Q_{xz,x}^s + Q_{yz,y}^s + N(w) &= 0 \end{aligned} \quad (12)$$

The equilibrium equation of a perfect FGP may be expressed as

$$\begin{aligned} N_{xx,xx} + N_{yy,yy} + 2N_{xy,xy} &= 0 \\ M_{xx,xx}^b + M_{yy,yy}^b + 2M_{xy,xy}^b + N(w) &= 0 \\ M_{xx,xx}^s + M_{yy,yy}^s + 2M_{xy,xy}^s + Q_{xz,x}^s + Q_{yz,y}^s + N(w) &= 0 \end{aligned} \quad (13)$$

When substituting the equation (10) into the equation (13), the governing equations can be degenerated as

$$\begin{aligned} D_b \nabla^4 w_b + D_s \nabla^4 w_s - N(w) &= 0 \\ D_s \nabla^4 w_b + H_s \nabla^4 w_s - A_s \nabla^2 w_s - N(w) &= 0 \end{aligned} \quad (14)$$

where

$$\begin{aligned} N(w) &= N_{xx}^0 \frac{d^2}{dx^2} (w_b + w_s) + N_{yy}^0 \frac{d^2}{dy^2} (w_b + w_s) \\ &\quad + 2N_{xy}^0 \frac{d^2}{dxdy} (w_b + w_s) \\ \nabla^2 &= \frac{d^2}{dx^2} + \frac{d^2}{dy^2} \quad \text{and} \quad \nabla^4 = \frac{d^4}{dx^4} + \frac{d^4}{dy^4} + 2 \frac{d^4}{dx^2 dy^2} \end{aligned}$$

To incorporate the geometric imperfection in the FGP, the imperfection function  $w^*(x, y)$  has been added to the displacement component  $w$ . To consider imperfection, the displacement component  $w_b + w_s$  shown in equation (14) must be replaced by  $w_b + w_s + w^*$ . Hence, the equilibrium equation (14) are modified as<sup>6</sup>

$$\begin{aligned} D_b \nabla^4 w_b + D_s \nabla^4 w_s - N_1(w) &= 0 \\ D_s \nabla^4 w_b + H_s \nabla^4 w_b - A_s \nabla^2 w_s - N_1(w) &= 0 \end{aligned} \quad (15)$$

where

$$\begin{aligned} N(w) &= N_{xx}^0 \frac{d^2}{dx^2} (w_b + w_s + w^*) \\ &\quad + N_{yy}^0 \frac{d^2}{dy^2} (w_b + w_s + w^*) \\ &\quad + 2N_{xy}^0 \frac{d^2}{dxdy} (w_b + w_s + w^*) \end{aligned}$$

Let us presume that the state of equilibrium of FGP subjected to load is using displacement components  $(u^0, v^0, w_b^0, w_s^0)$ . The displacement element of a neighboring state of stable equilibrium differs by  $(u^1, v^1, w_b^1, w_s^1)$  and  $w_1$  to the equilibrium position. Thus, the total displacement of a neighboring state is

$$\begin{aligned} u &= u^0 + u^1, v = v^0 + v^1, w_b = w_b^0 + w_b^1 \\ w_s &= w_s^0 + w_s^1 \end{aligned} \quad (16)$$

Correspondingly, the force resultant of a neighboring state can be related to the state of equilibrium as<sup>15,16</sup>

$$\begin{aligned} N_{xx} &= N_{xx}^0 + \Delta N_{xx} \quad N_{yy} = N_{yy}^0 + \Delta N_{yy} \\ N_{xy} &= N_{xy}^0 + \Delta N_{xy} \end{aligned} \quad (17)$$

where  $\Delta N_{xx}$ ,  $\Delta N_{yy}$ , and  $\Delta N_{xy}$  are the increment corresponding to  $(u^1, v^1 \text{ and } w_b^1, w_s^1)$  respectively. Now, let  $N_{xx}^1, N_{yy}^1$  and  $N_{xy}^1$  indicate the parts of  $\Delta N_x, \Delta N_y$  and  $\Delta N_{xy}$  that is linear in  $(u^1, v^1 \text{ and } w_b^1, w_s^1)$ . Regarding linear force addition, the above relation is written as follows

$$\begin{aligned} N_{xx} &= N_{xx}^0 + \Delta N_{xx}^1 \quad N_{yy} = N_{yy}^0 + \Delta N_{yy}^1 \\ N_{xy} &= N_{xy}^0 + \Delta N_{xy}^1 \end{aligned} \quad (18)$$

The stability equations are obtained by substituting equations (16) and (18) in equation (15). In the above equations, the temperature variation varies linearly along  $x$ - and  $y$ -direction. Subscript 0 represents the equilibrium condition. The nonlinear term with subscript 1 has been ignored because they are small compared to the linear terms. The remaining terms form the stability equations of imperfect FGP under load as follows

$$\begin{aligned} D_b \nabla^4 w_b^1 + D_s \nabla^4 w_s^1 - N_2(w) &= 0 \\ D_s \nabla^4 w_b^1 + H_s \nabla^4 w_s^1 - A_s \nabla^2 w_s^1 - N_2(w) &= 0 \end{aligned} \quad (19)$$

where

$$\begin{aligned} N_2(w) &= N_{xx}^0 \frac{d^2}{dx^2} (w_b^1 + w_s^1) + N_{yy}^0 \frac{d^2}{dy^2} (w_b^1 + w_s^1) \\ &\quad + 2N_{xy}^0 \frac{d^2}{dxdy} (w_b^1 + w_s^1) - N_{xx}^1 \frac{d^2}{dx^2} (w_b^0 + w_s^0 + w^*) + \\ &\quad N_{yy}^1 \frac{d^2}{dy^2} (w_b^0 + w_s^0 + w^*) + 2N_{xy}^1 \frac{d^2}{dxdy} (w_b^0 + w_s^0 + w^*) \end{aligned}$$

Again considering the first two equations of equation (12) for the stability condition.

$$\begin{aligned} N_{xx,x}^1 + N_{xy,x}^1 &= 0 \\ N_{yy,x}^1 + N_{xy,x}^1 &= 0 \end{aligned} \quad (20)$$

The subscript 0 and 1 symbolize the state of equilibrium and state of stability conditions respectively. Considering the equation (20), a stress function  $f$  may be expressed as<sup>6</sup>

$$N_{xx}^1 = f_{,yy} \quad N_{yy}^1 = f_{,xx} \quad N_{xy}^1 = -f_{,xy} \quad (21)$$

Substituting equation (21) into equation (19) leads to

$$\begin{aligned} D_b \nabla^4 w_b^1 + D_s \nabla^4 w_s^1 - N_3(w) &= 0 \\ D_s \nabla^4 w_b^1 + H_s \nabla^4 w_s^1 - A_s \nabla^2 w_s^1 - N_3(w) &= 0 \end{aligned} \quad (22)$$

where

$$\begin{aligned} N_3(w) &= N_{xx}^0 \frac{d^2}{dx^2} (w_b^1 + w_s^1) \\ &+ N_{yy}^0 \frac{d^2}{dy^2} (w_b^1 + w_s^1) + 2N_{xy}^0 \frac{d^2}{dxdy} (w_b^1 + w_s^1) \\ &+ f_{,yy} \left[ \frac{d^2}{dx^2} (w_b^0 + w_s^0 + w^*) \right] \\ &+ f_{,xx} \left[ \frac{d^2}{dy^2} (w_b^0 + w_s^0 + w^*) \right] \\ &- 2f_{,xy} \left[ \frac{d^2}{dxdy} (w_b^0 + w_s^0 + w^*) \right] \end{aligned}$$

This equation represents the stability equation of a geometrically imperfect FGP. Assume  $\varepsilon_{xx1}^0$ ,  $\varepsilon_{yy1}^0$  and  $\gamma_{xy1}^0$  indicates the parts of the strain element which are linear in  $(u_0^1, v_0^1$  and  $w_b^1, w_s^1)$ . These strains can be created in terms of the displacement components, applying equations (6), (16)–(18) with consideration of the imperfection term  $w^*$ , as<sup>25,26</sup>

$$\begin{aligned} \begin{Bmatrix} \varepsilon_{xx1}^0 \\ \varepsilon_{yy1}^0 \\ \gamma_{xy1}^0 \end{Bmatrix} &= \begin{Bmatrix} u_{0,x}^1 \\ v_{0,x}^1 \\ u_{0,y}^1 \end{Bmatrix} + \begin{Bmatrix} 0 \\ 0 \\ v_{0,x}^1 \end{Bmatrix} \\ \begin{Bmatrix} (w_{b,x}^0 + w_{s,x}^0 + w_{,x}^*) (w_{b,x}^1 + w_{s,x}^1) \\ (w_{b,y}^0 + w_{s,y}^0 + w_{,y}^*) (w_{b,y}^1 + w_{s,y}^1) \\ (w_{b,x}^0 + w_{s,x}^0 + w_{,x}^*) (w_{b,y}^1 + w_{s,y}^1) \end{Bmatrix} & \quad (23) \\ + \begin{Bmatrix} 0 \\ 0 \\ (w_{b,y}^0 + w_{s,y}^0 + w_{,y}^*) (w_{b,x}^1 + w_{s,x}^1) \end{Bmatrix} & \end{aligned}$$

Using equation (23), the geometrical compatibility equation is written as<sup>6</sup>

$$\begin{aligned} \varepsilon_{xx1,yy}^0 + \varepsilon_{yy1,xx}^0 - \gamma_{xy1,xy}^0 &= 2(w_{b,xy}^0 + w_{s,xy}^0 + w_{,xy}^*) \\ (w_{b,xy}^1 + w_{s,xy}^1) - (w_{b,yy}^0 + w_{s,yy}^0 + w_{,yy}^*) &(w_{b,xx}^1 + w_{s,xx}^1) \\ - (w_{b,xx}^0 + w_{s,xx}^0 + w_{,xx}^*) &(w_{b,yy}^1 + w_{s,yy}^1) \end{aligned} \quad (24)$$

From the constitutive relations (10a), one can write

$$\begin{aligned} \varepsilon_{xx1}^0 &= \frac{1}{E_1} (N_{xx1} - \nu N_{yy1} - E_2 K_{xx1}^b - I_1 K_{xx1}^s + \phi_{11}) \\ \varepsilon_{yy1}^0 &= \frac{1}{E_1} (N_{yy1} - \nu N_{xx1} - E_2 K_{yy1}^b - I_1 K_{yy1}^s + \phi_{11}) \\ \gamma_{xy1}^0 &= \frac{2}{E_1} [(1 + \nu) N_{xy1} - E_2 K_{xy1}^b - I_1 K_{xy1}^s] \end{aligned} \quad (25)$$

Substituting the above equations in equation (24), with the aid of equation (21), leads to the compatibility equation of an imperfect FGP

$$\frac{1}{E_1} \nabla^4 f - N_4(w) = 0 \quad (26)$$

where

$$\begin{aligned} N_4(w) &= 2 \left[ \frac{d^2}{dxdy} (w_b^1 + w_s^1) \right] \left[ \frac{d^2}{dxdy} (w_b^0 + w_s^0 + w^*) \right] \\ &- \left[ \frac{d^2}{dx^2} (w_b^1 + w_s^1) \right] \left[ \frac{d^2}{dy^2} (w_b^0 + w_s^0 + w^*) \right] - \\ &\left[ \frac{d^2}{dy^2} (w_b^1 + w_s^1) \right] \left[ \frac{d^2}{dx^2} (w_b^0 + w_s^0 + w^*) \right] \end{aligned}$$

Equations (15), (22), and (26) are the basic equations used to obtain the critical buckling load of an imperfect FGP.

## Mechanical buckling analysis

### Boundary conditions and final expression for critical buckling load

Assume a rectangular imperfect porous plate made of functionally graded materials with simply supported boundary conditions under in-plane loading in two directions as shown in Figures 1 and 2. The boundary conditions are defined as<sup>15,16</sup>

$$\begin{aligned} u = v = w = M_x = 0 \quad \text{on} \quad x = 0, a \\ u = v = w = M_y = 0 \quad \text{on} \quad y = 0, b \end{aligned} \quad (27)$$

The buckling forces are calculated by solving the equilibrium equation (15). These forces are obtained as<sup>15,16</sup>

$$N_{xx}^0 = -\frac{\delta_x}{b} \quad N_{yy}^0 = -\frac{\delta_y}{a} \quad N_{xy}^0 = 0 \quad (28)$$

The geometric imperfection function in the transverse direction has been added using the following expression.<sup>9,10</sup> The various modes of geometric imperfection have been shown in Figure 3.

$$\begin{aligned} w^*(x, y) &= \mu h \operatorname{sech}[\delta_1(x/a - \psi_1)] \\ &\cos[\mu_1 \pi(x/a - \psi_1)] \operatorname{sech}[\delta_2(y/b - \psi_2)] \\ &\cos[\mu_2 \pi(y/b - \psi_2)] \end{aligned} \quad (29)$$

where the coefficient  $\mu$  varies in the range of 0 to 1.

The following analytical solution is seen to satisfy both the equilibrium equation (15) and the edge conditions represented by equation (27)<sup>14</sup>

$$\begin{aligned} w_b^0(x, y) &= \sum_{m=1}^{\infty} \sum_{n=1}^{\infty} B_{mn} \sin \frac{m\pi x}{a} \sin \frac{n\pi y}{b} \\ m, n &= 1, 2, \dots \\ w_s^0(x, y) &= \sum_{m=1}^{\infty} \sum_{n=1}^{\infty} S_{mn} \sin \frac{m\pi x}{a} \sin \frac{n\pi y}{b} \end{aligned} \quad (30)$$

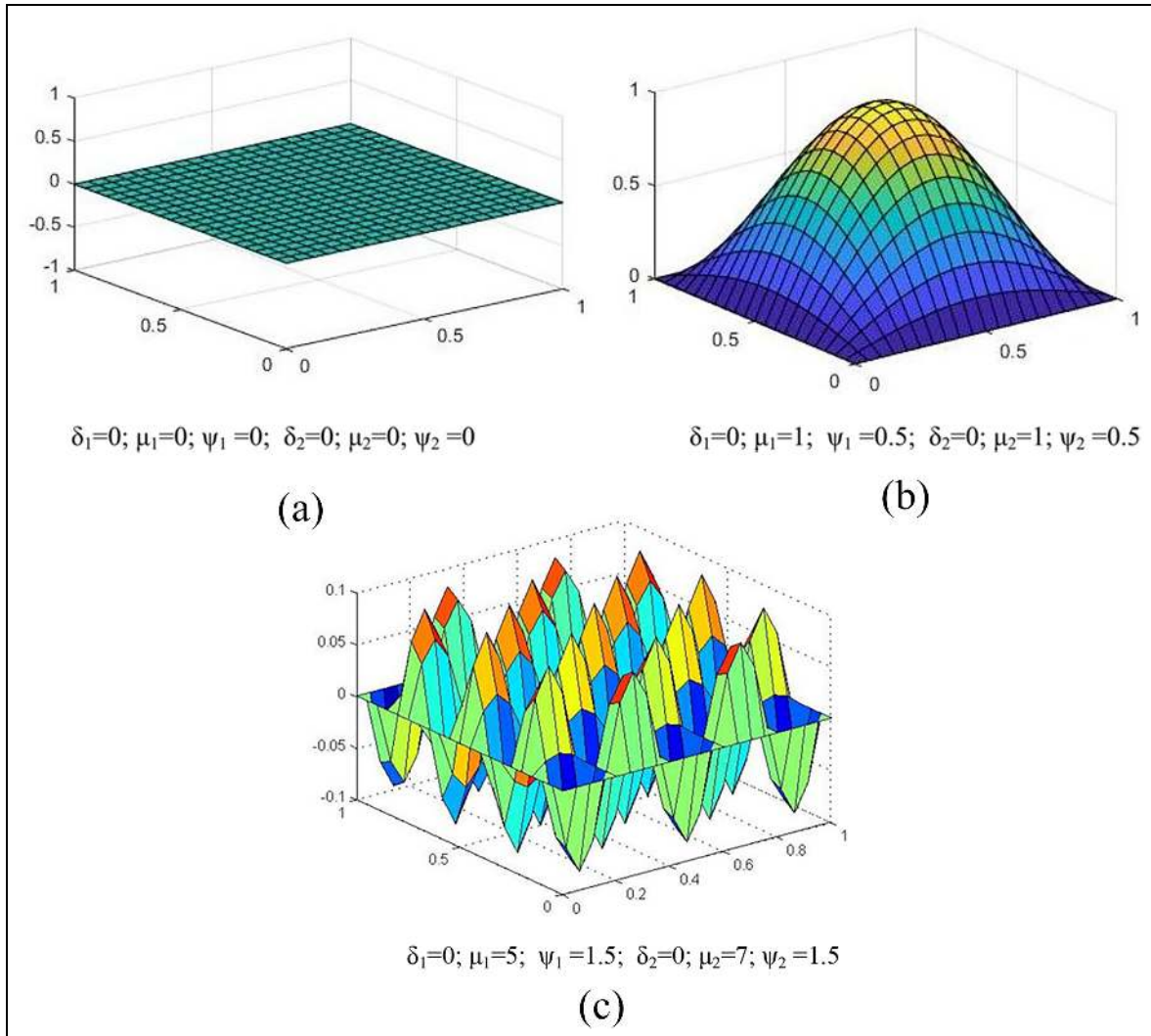


**Figure 3.** Perfect and geometrically imperfect FGP: (a) perfect FGP, (b) sine type geometrically imperfect FGP, and (c) global type imperfection (GI).

From equation (15),

$$\begin{aligned} B_{mn} &= C S_{mn} \\ w_b^0(x, y) &= C w_s^0(x, y) \end{aligned} \quad (31)$$

where

$$C = \frac{(H_s - D_s)(\alpha^2 + \beta^2) + A_s}{(D_b - D_s)(\alpha^2 + \beta^2)} \quad (32)$$

where,  $B_{mn}$  and  $S_{mn}$  is a constant coefficient. Substituting equations (28)–(31) into the third equilibrium equation (15), the constant  $S_{mn}$  is obtained and the final approximate solution can be written as

$$w_s^0(x, y) = \frac{\left(-\frac{\delta_x}{b}\right)(w_{,xx}^* + \gamma w_{,yy}^*)}{(CD_b + D_s)(\alpha^2 + \beta^2)^2 - \frac{\delta_x}{b}(\alpha^2 + \gamma\beta^2)[1 + C]} \sin \alpha x \sin \beta y \quad (33)$$

where

$$\alpha = \frac{m\pi}{a}, \quad \beta = \frac{n\pi}{b}, \quad \gamma = \left(\frac{\delta_y}{\delta_x}\right) \left(\frac{b}{a}\right)$$

Here,  $\gamma$  is a load ratio non-dimensional constant that relates one independent load parameter to another.

To solve both equations (22) and (26) with the adding of the boundary conditions (27), the approximate solutions can be considered as

$$\begin{aligned} w_b^1(x, y) &= \sum_{m=1}^{\infty} \sum_{n=1}^{\infty} W_{bmn} \sin \alpha x \sin \beta y \\ w_s^1(x, y) &= \sum_{m=1}^{\infty} \sum_{n=1}^{\infty} W_{smn} \sin \alpha x \sin \beta y \quad m, n = 1, 2, \\ f(x, y) &= \sum_{m=1}^{\infty} \sum_{n=1}^{\infty} F_{mn} \sin \alpha x \sin \beta y \end{aligned} \quad (34)$$

Using equation (19)

$$\begin{aligned} W_{bmn} &= C W_{smn} \\ w_b^1(x, y) &= C w_s^1(x, y) \end{aligned} \quad (35)$$

where  $W_{bmn}$ ,  $W_{smn}$  and  $F_{mn}$  are constant coefficients that depend on  $m$  and  $n$ . Substituting approximate solutions (28), (34), and (35) into both equations (22) and (26), we get

$$D_b(\alpha^2 + \beta^2)^2 C w_s^1 + D_s(\alpha^2 + \beta^2)^2 w_s^1 - N_{mn}^*(w) = 0 \quad (36a)$$

where

$$\begin{aligned} N_{mn}^*(w) &= \left(-\frac{\delta_x}{b}\right) \frac{d^2}{dx^2} [(C+1)w_s^1] \\ &+ \gamma \left(-\frac{\delta_x}{b}\right) \frac{d^2}{dy^2} [(C+1)w_s^1] - H_{mn}^* F_{mn} \end{aligned} \quad (36b)$$

$$\frac{1}{E_1}(\alpha^2 + \beta^2)^2 f - H_{mn}^* W_{smn}(C+1) = 0$$

$$\begin{aligned} R_1 &= D_b(\alpha^2 + \beta^2)^2 C W_{smn} \sin \alpha x \sin \beta y \\ &+ D_s(\alpha^2 + \beta^2)^2 W_{smn} \sin \alpha x \sin \beta y \\ &- \left(\frac{\delta_x}{b}\right) (\alpha^2 + \gamma\beta^2) [(C+1)W_{smn} \sin \alpha x \sin \beta y] + H_{mn}^* F_{mn} \end{aligned}$$

$$R_2 = \frac{1}{E_1}(\alpha^2 + \beta^2)^2 F_{mn} \sin \alpha x \sin \beta y - H_{mn}^* W_{smn}(C+1) \quad (37)$$

where  $R_1$  and  $R_2$  are the residues of the equation (36), which can be solved by the Galerkin's method after taking the orthogonally concerning the approximate solutions as<sup>6</sup>

$$\begin{aligned} \int_0^a \int_0^b R_1 \sin \alpha x \sin \beta y dx dy &= 0 \\ \int_0^a \int_0^b R_2 \sin \alpha x \sin \beta y dx dy &= 0 \end{aligned} \quad (38)$$

The determinant of the system of equation (38) for the coefficients  $W_{bmn}$  and  $W_{smn}$  is set to zero, which obtained the implicit expression for imperfect porous FGM plate

$$\frac{\delta_{cr}}{b} = \frac{(CD_b + D_s)(\alpha^2 + \beta^2)^2 + S1^2 * S2}{(\alpha^2 + \gamma\beta^2)[C+1]} \quad (39)$$

where

$$\begin{aligned} S1 &= \int_0^a \int_0^b H_{mn}^* \sin \alpha x \sin \beta y dx dy \\ S2 &= \frac{E_1(C+1)}{\left\{(\alpha^2 + \beta^2)^2 \left(\frac{ab}{4}\right)^2\right\}} \end{aligned}$$

$$\begin{aligned} H_{mn}^* &= \left\{ \alpha^2 \left[ \frac{d^2}{dy^2} [(C+1)w_s^0 + w^*] \right] \right. \\ &+ \beta^2 \left[ \frac{d^2}{dx^2} [(C+1)w_s^0 + w^*] \right] \left. \right\} \sin \alpha x \sin \beta y \\ &+ 2\alpha\beta \left[ \frac{d^2}{dx dy} [(C+1)w_s^0 + w^*] \right] \cos \alpha x \cos \beta y \end{aligned}$$

If the sinusoidal type of geometric imperfection<sup>6</sup> has been used, the explicit expression for critical buckling load of imperfect porous FGP can be given as

$$\frac{\delta_{cr}}{b} = \frac{(CD_b + D_s)(\alpha^2 + \beta^2)^2 + (H_{mn})^{1/3}}{(\alpha^2 + \gamma\beta^2)[C+1]} \quad (40)$$

where

$$H_{mn} = \frac{1024(C+1)\alpha^2\beta^2 E_1(\mu h)^2 D^2(\alpha^2 + \beta^2)^2 [CD_b + D_s]^2}{9a^2 b^2}$$

Note that these equations are calculated for odd values of  $m$  and  $n$ . The critical buckling load is the smallest value of the given values of the load ratio  $\gamma$  and the aspect ratio  $\psi(a/b)$ . When substituting  $\mu = 0$ , the imperfection term  $H_{mn}$  is zero, and equation (40) is reduced to the buckling of a perfect FGP.

$$\frac{\delta_{cr}}{b} = \frac{(CD_b + D_s)(\alpha^2 + \beta^2)^2}{(\alpha^2 + \gamma\beta^2)[C+1]} \quad (41)$$

where

$$\begin{aligned} D_s &= \frac{(I_2 E_1 - E_2 I_1)}{E_1(1 - \nu^2)}, & D_b &= \frac{E_1 E_3 - E_2^2}{E_1(1 - \nu^2)}, \\ H_s &= \frac{E_1 I_3 - I_2^2}{E_1(1 - \nu^2)}, & A_s &= \frac{I_4}{2(1 + \nu)} \end{aligned}$$

$$[E_1 \quad E_2 \quad E_3] = \int_{-h/2}^{h/2} E(z) [1 \quad z \quad z^2] dz$$

$$[I_1 \quad I_2 \quad I_3 \quad I_4] = \int_{-h/2}^{h/2} E(z) L [1 \quad z \quad L \quad \frac{z^2(z)}{L}] dz$$

## Thermal buckling analysis

A fixed-simply supported FGP is assumed to be under thermal loading. The edge conditions are<sup>15,16</sup>

$$\begin{aligned} u = v = w = M_x = 0 \quad \text{on} \quad x = 0, a \\ u = v = w = M_y = 0 \quad \text{on} \quad y = 0, b \end{aligned} \quad (42)$$

The prebuckling resultant forces are defined as<sup>15,16</sup>

$$N_{xx}^0 = -\frac{\phi_1}{1 - \nu} \quad N_{yy}^0 = -\frac{\phi_1}{1 - \nu} \quad N_{xy}^0 = 0 \quad (43)$$

where, the thermal parameter  $\phi_1$  is given by equation (11). Substituting equations (29)–(31) and (43) in the



equilibrium equation (15), the prebuckling deflection  $w_0$  subjected to the thermal load is obtained as

$$w_{sT}^0(x, y) = \frac{\left(-\frac{\phi_1}{(1-\nu)}\right)(w_{,xx}^* + w_{,yy}^*)}{(CD_b + D_s)(\alpha^2 + \beta^2)^2 - \left(\frac{\phi_1}{(1-\nu)}\right)(\alpha^2 + \beta^2)[1 + C]} \sin \alpha x \sin \beta y \quad (44)$$

Similar to the above-discussed solution procedure, substitution of equations (29), (43), and (44) in equations (22) and (26) yields a set of three differential equations with three incremental variables  $w^1$ ,  $f$  and  $u_{0,x}^1 + u_{0,x}^1$ . Using the approximate function given in equations (34), with equations (22) and (26), the residue has been made orthogonal. Finally, the implicit equations of the unknown thermal parameter  $\phi_1$  is calculated as

$$\frac{\phi_1}{(1-\nu)} = \frac{(CD_b + D_s)(\alpha^2 + \beta^2)^2 + S1_T^2 * S2_T}{(\alpha^2 + \beta^2)[C + 1]} \quad (45a)$$

$$S1_T = \int_0^a \int_0^b H_{mnT}^* \sin \alpha x \sin \beta y dx dy$$

$$S2_T = \frac{E_1(C + 1)}{\{(\alpha^2 + \beta^2)^2 \left(\frac{ab}{4}\right)^2\}}$$

$$H_{mnT}^* = \left\{ \alpha^2 \left[ \frac{d^2}{dy^2} [(C + 1)w_{sT}^0 + w^*] \right] \right.$$

$$+ \beta^2 \left[ \frac{d^2}{dx^2} [(C + 1)w_{sT}^0 + w^*] \right] \left. \right\} \sin \alpha x \sin \beta y$$

$$+ 2\alpha\beta \left[ \frac{d^2}{dx dy} [(C + 1)w_{sT}^0 + w^*] \right] \cos \alpha x \cos \beta y$$

If the sinusoidal type of geometric imperfection function<sup>6</sup> has been used, the explicit expression for critical buckling temperature of imperfect porous FGP can be given as

$$\frac{\phi_1}{(1-\nu)} = \frac{(CD_b + D_s)(\alpha^2 + \beta^2)^2 + (H_{mn})^{1/3}}{(\alpha^2 + \beta^2)[C + 1]} \quad (45b)$$

### Uniform temperature rise

The initial temperature is considered  $T_i$ . The temperature is uniformly raised to a final value  $T_f$ . The temperature change is  $\Delta T = T_f - T_i$ . Using equations (1), (11), and (45), the buckling temperature change is calculated as

$$\Delta T_{Ucr} = \frac{\phi_1}{L_U} \quad (46)$$

**Table 1.** Various properties of FGMs.<sup>11,25</sup>

Material	Material properties	
	Young's modulus (GPa)	Thermal expansion ( $\alpha_T$ )
Al	70	$23 \times 10^{-6}$
Al <sub>2</sub> O <sub>3</sub>	380	$7.4 \times 10^{-6}$
SiC	420	$4.4 \times 10^{-6}$

where

$$L_U = \int_{-h/2}^{h/2} E(z) \cdot \alpha_T(z) dz \quad (47)$$

The critical buckling temperature change  $\Delta T_{Ucr}$  is the smallest value of  $\Delta T$ . It is clear from equation (34), and equation (45) that the  $\Delta T_{Ucr}$  can be obtained after substituting  $m = 1$  and  $n = 1$  in equation (46). Substituting  $\mu = 0$  or  $k = 0$ , equation (46) is reduced to  $\Delta T_{Ucr}$  for a perfect FGP or a homogenous imperfect plate respectively.

### Buckling of imperfect FGP under linear longitudinal temperature change

Assume a linear temperature variation along the  $x$ -direction as<sup>25,26</sup>

$$T(x) = \Delta T \left( \frac{x}{a} \right) + T_0 \quad 0 \leq x \leq a \quad (48)$$

where

$$\Delta T = T_a - T_0$$

Here,  $T_a$  and  $T_0$  are the temperature at sides  $x = a$  and  $x = 0$ , respectively. Following a similar procedure,  $\Delta T_{Lcr}$  is derived as

$$\Delta T_{Lcr} = 2\Delta T_{Ucr} \quad (49)$$

## Numerical results and discussion

To examine the effectiveness of the current exact expression, several illustrations of the thermal and mechanical buckling response of FGPs have been presented in this section. The subsequent section has been divided into two parts. In the first part, validation studies have been given whereas in the second part, new results have been provided. The influence of geometric configurations, porosity inclusion, geometric imperfection, and power-law index on the stability of FGPs have been investigated. The material properties of FGPs are listed in Table 1.

**Table 2.** Comparison of the critical buckling load  $\delta_{cr}(MN)$  of simply supported Al/Al<sub>2</sub>O<sub>3</sub> perfect plate subjected to different kinds of loading versus side-to-thickness ratio  $\phi(a/h)$  ( $\psi = 0.5, k = 1, \mu = 0, \lambda = 0$ ).

$\gamma$	Method	Side-to-thickness ratio $\phi(a/h)$					
		5	10	20	30	40	50
0	Present	239.490	32.485	4.149	1.234	0.521	0.267
	CPT <sup>8</sup>	267.480 (10.464)*	33.435 (2.841)	4.179 (0.717)	1.238 (0.323)	0.522 (0.191)	0.267 (0.000)
	FSDT <sup>18</sup>	243.410 (1.610)*	32.628 (0.438)	4.154 (0.120)	1.235 (0.080)	0.522 (0.191)	0.268 (0.373)
	HSDT <sup>31</sup>	239.150 (0.142)*	32.472 (0.040)	4.149 (0.000)	1.234 (0.000)	0.522 (0.191)	0.267 (0.000)
	Thai and Choi <sup>14</sup>	239.145 (0.144)*	32.472 (0.039)	4.148 (0.024)	1.234 (0.000)	0.521 (0.000)	0.267 (0.000)
I	Present	191.592	25.988	3.319	0.987	0.417	0.214
	CPT <sup>8</sup>	213.990 (10.467)*	26.748 (2.841)	3.435 (3.337)	0.990 (0.303)	0.417 (0.000)	0.214 (0.000)
	FSDT <sup>18</sup>	194.730 (1.611)*	26.103 (0.441)	3.323 (0.120)	0.988 (0.101)	0.417 (0.000)	0.213 (0.140)
	HSDT <sup>31</sup>	191.320 (0.142)*	25.978 (0.038)	3.318 (0.003)	0.987 (0.000)	0.417 (0.000)	0.213 (0.140)
	Thai and Choi <sup>14</sup>	191.316 (0.144)*	25.977 (0.040)	3.318 (0.003)	0.987 (0.000)	0.417 (0.000)	0.213 (0.140)
-I	Present	319.320	43.313	5.532	1.646	0.695	0.356
	CPT <sup>8</sup>	356.640 (10.464)*	44.580 (2.842)	5.572 (0.717)	1.6511 (0.308)	0.696 (0.143)	0.356 (0.000)
	FSDT <sup>18</sup>	324.540 (1.608)*	43.505 (0.441)	5.538 (0.108)	1.646 (0.000)	0.695 (0.000)	0.356 (0.000)
	HSDT <sup>31</sup>	318.860 (0.144)*	43.296 (0.039)	5.531 (0.018)	1.645 (0.060)	0.695 (0.000)	0.356 (0.000)
	Thai and Choi <sup>14</sup>	318.860 (0.144)*	43.296 (0.039)	5.531 (0.018)	1.645 (0.060)	0.695 (0.000)	0.356 (0.000)

\*In parenthesis %difference =  $\frac{\text{Reference} - \text{Present}}{\text{Reference}} \times 100$ .

**Table 3.** Comparison of the critical buckling loads  $\delta_{cr}(10^3KN)$  for a simply-supported Al/Al<sub>2</sub>O<sub>3</sub> perfect plate subjected to different kinds of loading versus the side-to-thickness ratio  $\Phi(b/h)$ .

$\gamma$	Method	Side-to-thickness ratio $\Phi(b/h)$		
		10	20	100
0	Present	239.490	32.485	0.267
	Shariat and Eslami <sup>18</sup>	243.410 (1.610)*	32.628 (0.438)	0.267 (0.000)
	Mohammadi et al. <sup>11</sup>	243.407 (1.609)*	32.628 (0.439)	0.267 (0.000)
I	Present	191.592	25.988	0.214
	Shariat and Eslami <sup>18</sup>	194.730 (1.611)*	26.103 (0.440)	0.213 (0.469)
	Mohammadi et al. <sup>11</sup>	194.725 (1.609)*	26.102 (0.437)	0.213 (0.469)
-I	Present	319.320	43.313	0.356
	Shariat and Eslami <sup>18</sup>	324.540 (1.608)*	43.505 (0.441)	0.356 (0.000)
	Mohammadi et al. <sup>11</sup>	324.542 (1.609)*	43.504 (0.440)	0.356 (0.000)

\*In parenthesis %difference =  $\frac{\text{Reference} - \text{Present}}{\text{Reference}} \times 100$ .

**Validation studies**

Example 1: In the first example, the buckling analysis of a simply-supported Al/Al<sub>2</sub>O<sub>3</sub> perfect FGP is studied and compared with the results presented by Thai and Choi.<sup>14</sup> The side-to-thickness ratio  $\phi(a/h)$  varies from 5 to 50 and FGP is subjected to various loading conditions. It is observed from Table 2, that the percentage difference between the current outcomes and the referred results are 0–10.50%, 0–1.62%, and 0–0.15% for CPT,<sup>8</sup> FSDT,<sup>18</sup> and HSDT<sup>31</sup> respectively for all the side to thickness ratio  $\phi$  under various loading conditions. The present results are in good agreement with the reported results.

Example 2: In the second example, the critical buckling loads  $\delta_{cr}$  of simply-supported perfect Al/Al<sub>2</sub>O<sub>3</sub> rectangular FGP are represented in Table 3. The computed results are compared with those presented by Mohammadi et al.<sup>11</sup> and Shariat and Eslami.<sup>18</sup> In both the reported papers, authors have presented the exact solution for buckling response based on higher-order

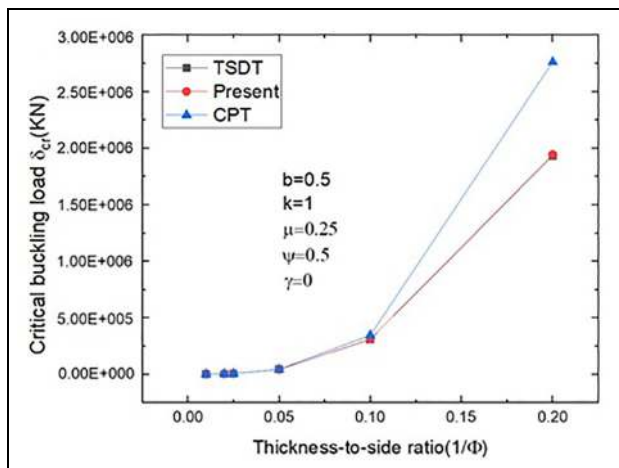


**Figure 4.** Comparison of critical buckling load  $\delta_{cr}(N)$  of simply-supported Al/Al<sub>2</sub>O<sub>3</sub> FGP with geometric imperfection and non-porous subjected to uniaxial compression versus thickness-to-side ratio.

**Table 4.** Critical buckling load  $\delta_{cr}(10^3KN)$  of Al/SiC FGP ( $\mu = 0, \lambda = 0$ ) versus  $\phi$  ratio with power-law index  $k$  subjected to different kinds of loading ( $\gamma = 0, 1, -1, \psi = 0.5$ ).

$\gamma$	$k$	Side-to-thickness ratio ( $\phi$ )				
		5	10	20	40	50
0	Ceramic	520.813	71.650	9.188	1.156	0.592
	1	257.478	34.887	4.455	0.560	0.287
	5	155.450	21.881	2.825	0.356	0.182
	10	138.775	19.810	2.568	0.324	0.166
	Metal	106.212	14.822	1.908	0.240	0.123
1	Ceramic	416.651	57.320	7.350	0.925	0.474
	1	205.983	27.910	3.564	0.448	0.229
	3	124.360	17.505	2.260	0.285	0.146
	10	111.020	15.848	2.054	0.259	0.133
	Metal	84.969	11.858	1.527	0.192	0.099
-1	Ceramic	694.418	95.533	12.250	1.541	0.790
	1	343.305	46.516	5.939	0.746	0.382
	3	207.267	29.175	3.766	0.475	0.243
	10	185.033	26.413	3.424	0.432	0.221
	Metal	141.615	19.763	2.545	0.320	0.164

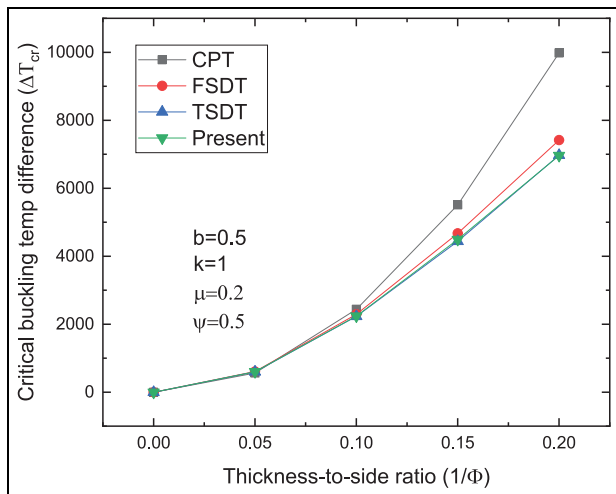


**Figure 5.** Critical buckling temp change  $\Delta T_{cr}$  of simply-supported Al/Al<sub>2</sub>O<sub>3</sub> imperfect FGP under uniform temp rise.

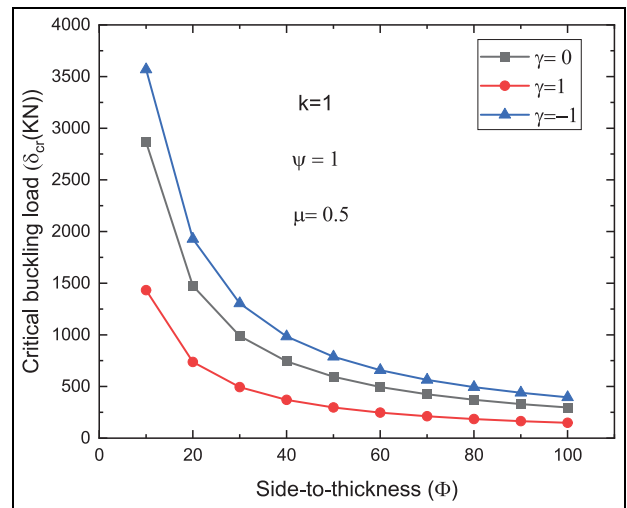


**Figure 6.** Critical buckling load  $\delta_{cr}$  of simply supported Al/SiC Sine-type geometrically imperfect non-porous FGP versus side-to-thickness ratio  $\phi$  with different load ( $h = 0.005$ ).

shear deformation theory (HSDT). It is observed that the percentage difference between the present results and reported results are approximately 0–1.62% for all the side to thickness ratio  $\Phi(b/h)$  under various loading conditions.

Example 3: In the third example, the comparison of the critical buckling load  $\delta_{cr}$  of geometrically imperfect FGP with the various thickness-to-side ratio ( $1/\Phi$ ) is illustrated in Figure 4, based on CPT, third-order shear deformation theory (TSDT),<sup>15</sup> and current HSDT. The non-porous geometrically imperfect FGP is investigated under in-plane uniaxial compression loading. It is noticed that the CPT overestimates the buckling load, especially for thick plate while TSDT and recent HSDT give the results very close to each other for thick as well as thin plates.

Example 4: In the last example, a comparison of the critical buckling temperature difference  $\Delta T_{cr}$  of non-porous geometrically imperfect FGPs versus various thickness-to-side ratio ( $1/\Phi$ ) subjected to uniform temperature rise is illustrated in Figure 5, using CPT,<sup>25</sup> FSDT,<sup>26</sup> TSDT,<sup>15</sup> and present HSDT. It can be seen that the current outcomes match excellently with TSDT.

**Numerical illustrations**

After validation of the present formulation, various numerical illustrations for the buckling analysis of Al/SiC have been examined in the following section. The influence of volume fraction index, porosity inclusions,

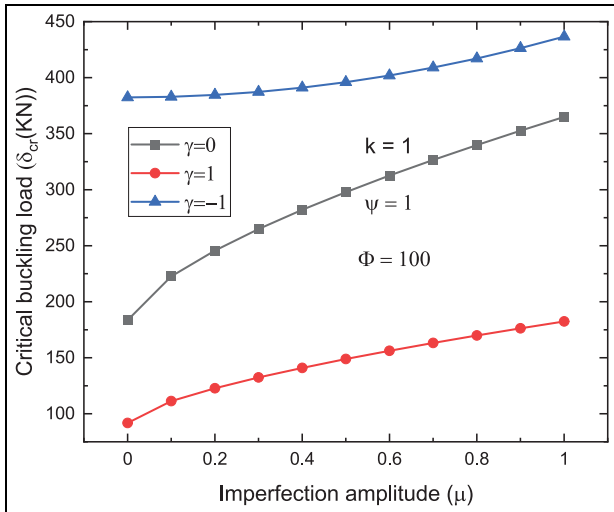


**Figure 7.** Critical buckling load  $\delta_{cr}$  of simply supported Al/SiC Sine-type geometrically imperfect non-porous FGP versus imperfection amplitude  $\mu$  with different load.

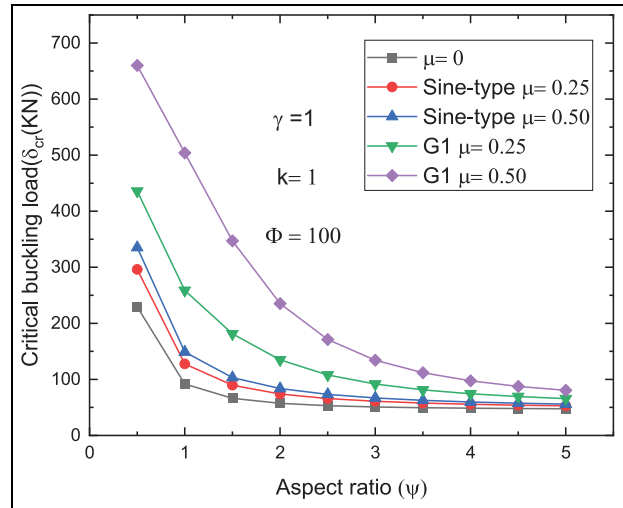


**Figure 9.** Critical buckling load  $\delta_{cr}$  of simply supported Al/SiC geometrically imperfect non-porous FGP under biaxial compression versus aspect ratio  $\psi$  with imperfection amplitude  $\mu$ .

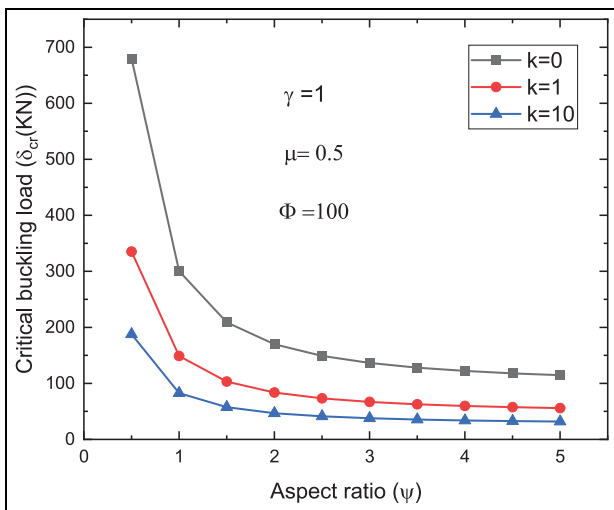


**Figure 8.** Critical buckling load  $\delta_{cr}$  of simply supported Al/SiC Sine-type geometrically imperfect non-porous FGP under biaxial compression versus aspect ratio  $\psi$  with power-law index  $k$ .

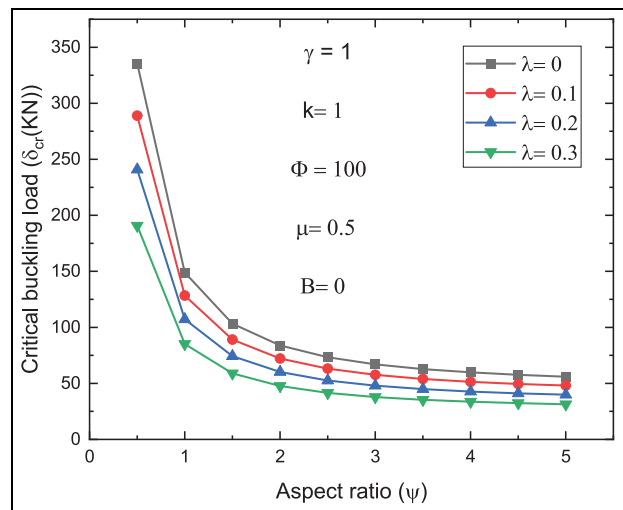


**Figure 10.** Critical buckling load  $\delta_{cr}$  of simply supported Al/SiC Sine-type geometrically imperfect porous FGP versus aspect ratio  $\psi$  with porosity index  $\lambda$  under biaxial compression ( $B = 0$ ).

geometric imperfection, and several loading conditions on the critical buckling load and critical buckling temperature have been investigated extensively.

Table 4 shows that the critical buckling load  $\delta_{cr}$  of perfect FGP under uniaxial compression ( $\gamma = 0$ ), biaxial compression ( $\gamma = 1$ ), and combined compression and tension ( $\gamma = -1$ ) are presented. It is noticed that the critical buckling load increases with decreasing the power-law index  $k$  as well as the side to thickness ratio  $\phi$ . It is expected because as the power-law index  $k$  decreases, metallic content in FGP decreases, consequently stiffness increases. On the other hand, as a side to thickness ratio  $\phi$  increases, the FGP is transfigured from thick to thin, therefore the stiffness decreases. The

critical buckling load for the perfect plates subjected to uniaxial compression is greater than biaxial compression and less than combined compression and tension.

Figures 6 and 7 present the variation of the critical buckling load  $\delta_{cr}$  of FGP with side-to-thickness ratio  $\phi$  and imperfection amplitude  $\mu$  respectively. It is evident from the results that the critical buckling load  $\delta_{cr}$  of geometrically imperfect porous FGP increases with the imperfection amplitude, whereas it decreases with an increase in the side-to-thickness ratio for all types of mechanical loadings. It is also observed that the critical buckling load  $\delta_{cr}$  is maximum and minimum for the FGP subjected to combined tension and compression, and bi-axial compression loading conditions,

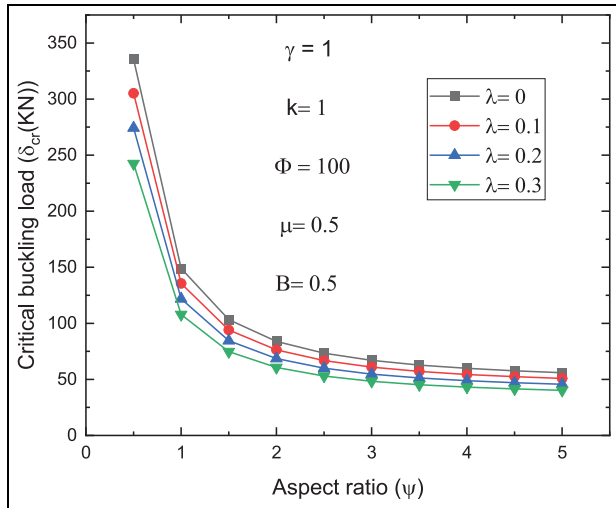


**Figure 11.** Critical buckling load  $\delta_{cr}$  of simply supported Al/SiC Sine-type geometrically imperfect porous FGP versus aspect ratio  $\psi$  with porosity index  $\lambda$  under biaxial compression ( $B = 0.5$ ).

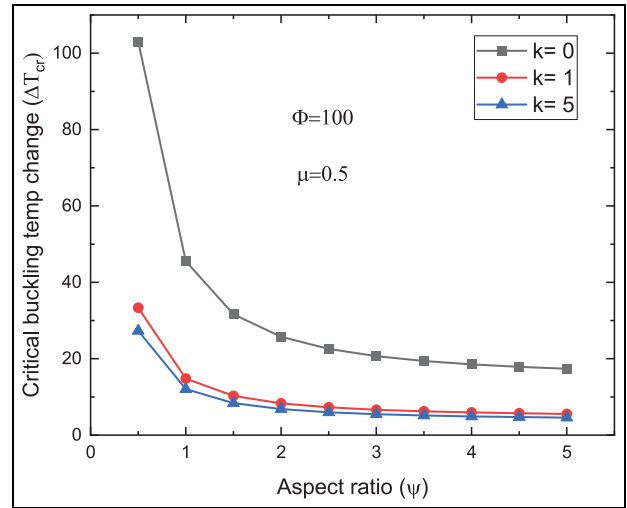


**Figure 13.** The critical buckling temperature change  $\Delta T_{cr}$  of simply-supported Al/SiC Sine-type geometrical imperfect non-porous FGP under uniform temp rise versus aspect ratio  $\psi$  and power-law index  $k$ .

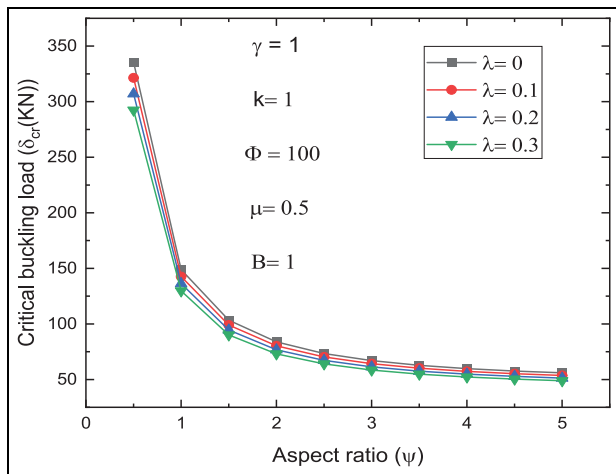


**Figure 12.** Critical buckling load  $\delta_{cr}$  of simply supported Al/SiC Sine-type geometrically imperfect porous FGP versus aspect ratio  $\psi$  with porosity index  $\lambda$  under biaxial compression ( $B = 1$ ).

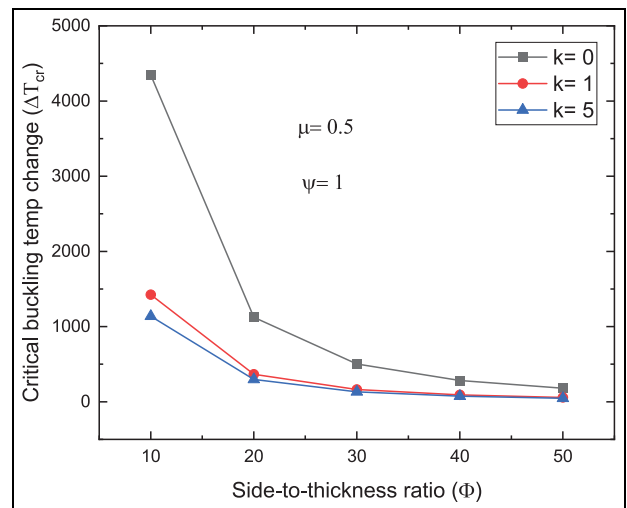


**Figure 14.** The critical buckling temperature change  $\Delta T_{cr}$  of simply-supported Al/SiC Sine-type geometrical imperfect non-porous FGP under uniform temp rise versus side-to-thickness ratio  $\Phi(b/h)$  and power-law index  $k$ .

respectively. It is found that as a side to thickness ratio increases from 10 to 100, the difference amongst the critical buckling load  $\delta_{cr}$  decreases under various mechanical loading. It is also noticed that for the combined tension and compression type of loading, the influence of geometric imperfection is least.

Figures 8 and 9 show that the critical buckling load  $\delta_{cr}$  of FGP under biaxial compression (side to thickness ratio and volume fraction index as 100 and 1, respectively) for different aspect ratio and modes of geometric imperfection. It is evident from Figure 8 that the critical buckling load  $\delta_{cr}$  for a metal plate ( $k > 0$ ) is lower than the fully ceramic ( $k = 0$ ) due to the higher stiffness of ceramic. It is clear from the results that as the aspect ratio  $\psi$  increases, the critical buckling load  $\delta_{cr}$  decreases monotonically for all the volume fraction index  $k$ . It is

noticed that the change in critical buckling load  $\delta_{cr}$  due to volume fraction index is more for the aspect ratio  $\psi$  up to 2.5. On the further increment in the aspect ratio, lead to marginal changes in the buckling load. In Figure 9, two-type of geometric imperfection modes that is, Global (G1) and Sine-type have been considered. It is evident that G1 type imperfection has more effect on the buckling behavior of FGP compared to Sine-type imperfection. It is notable that the critical buckling load  $\delta_{cr}$  increase when increasing the imperfection amplitude  $\mu$ .

Figures 10 to 12 illustrate the buckling response of porous FGP under bi-axial compression. The effective materials properties of porous FGP have been

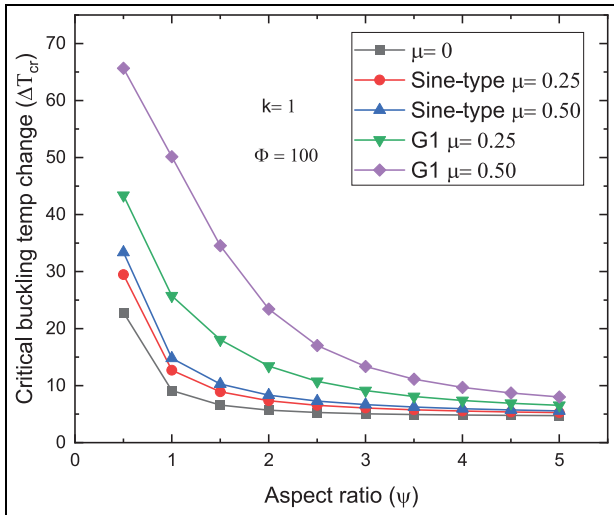


**Figure 15.** The critical buckling temperature change  $\Delta T_{cr}$  of simply-supported Al/SiC geometrical imperfect non-porous FGP under uniform temp rise versus aspect ratio  $\psi$  and imperfection size  $\mu$ .

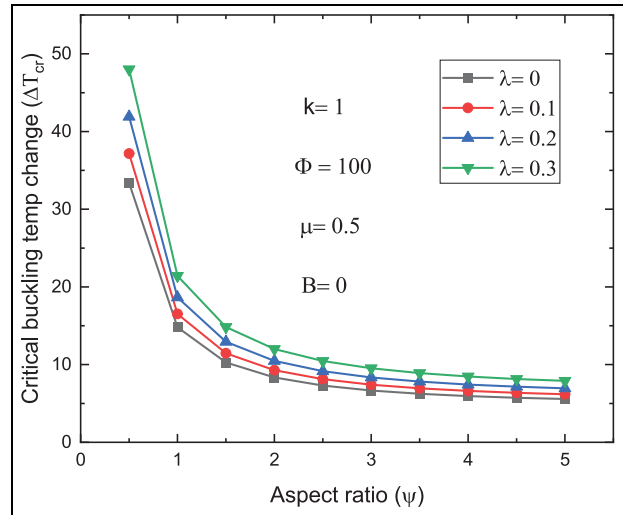


**Figure 17.** The critical buckling temperature change  $\Delta T_{cr}$  of simply-supported Al/SiC sinusoidal geometrical imperfect porous FGP under uniform temp rise versus aspect ratio  $\psi$  and porosity index  $\lambda$  ( $B = 0$ ).

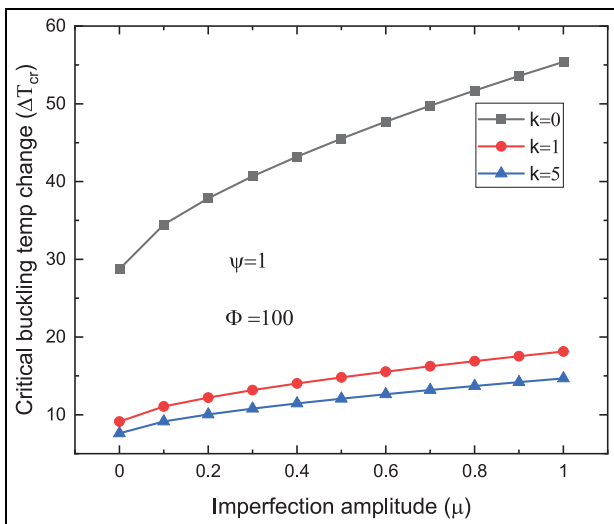


**Figure 16.** The critical buckling temperature change  $\Delta T_{cr}$  of simply-supported Al/SiC sinusoidal geometrical imperfect non-porous FGP under uniform temp rise versus imperfection size  $\mu$  and power-law index  $k$ .

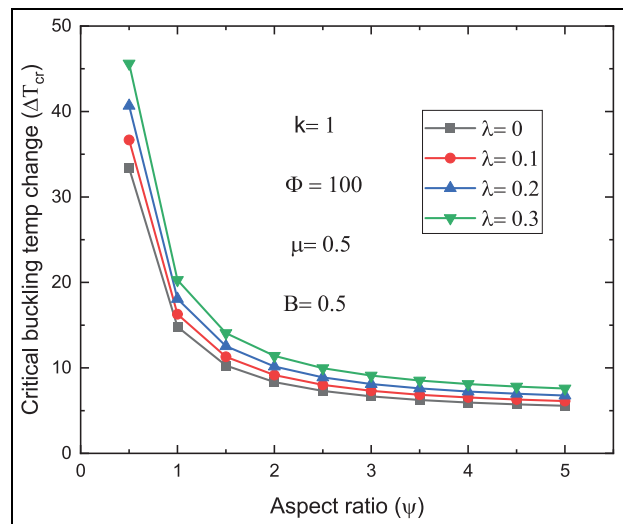


**Figure 18.** The critical buckling temperature change  $\Delta T_{cr}$  of simply-supported Al/SiC sinusoidal geometrical imperfect porous FGP under uniform temp rise versus aspect ratio  $\psi$  and porosity index  $\lambda$  ( $B = 0.5$ ).

estimated using equation (1). It is noteworthy that when  $B = 0$ , the FGP will be having even porosity distribution whereas for  $B = 1$ , FGP will possess uneven porosity distribution. It can be seen from the results that when the porosity volume fraction  $\lambda$  increases, the plate becomes more flexible therefore, the critical buckling load  $\delta_{cr}$  decreases. Critical buckling load  $\delta_{cr}$  increases as the porosity distribution changes form even ( $B = 0$ ) to uneven ( $B = 1$ ).

Figures 13 and 14 show that the variation of critical buckling Temperature change  $\Delta T_{cr}$  of geometrically imperfect non-porous FGP with volume fraction index  $k$ , side-to-thickness ratio  $\Phi$ , and aspect ratio  $\psi$  under

uniform temperature rise. It is clear from the results that  $\Delta T_{cr}$  increase with decreasing the aspect ratio  $\psi$ , side-to-thickness ratio  $\Phi$  as well as the volume fraction index  $k$ . The increment is marginal for aspect ratio and a side-to-thickness ratio  $\Phi$  greater than 3.5 and 30, respectively.

It is clear from Figures 15 and 16 that the critical buckling temperature change  $\Delta T_{cr}$  depends on the imperfection amplitude  $\mu$ . It is clear that the presence of geometric imperfection leads to an increase in the critical buckling temperature. Its value is maximum for G1 type of imperfection whereas minimum when the plate is geometrically perfect. It is also noticed that the

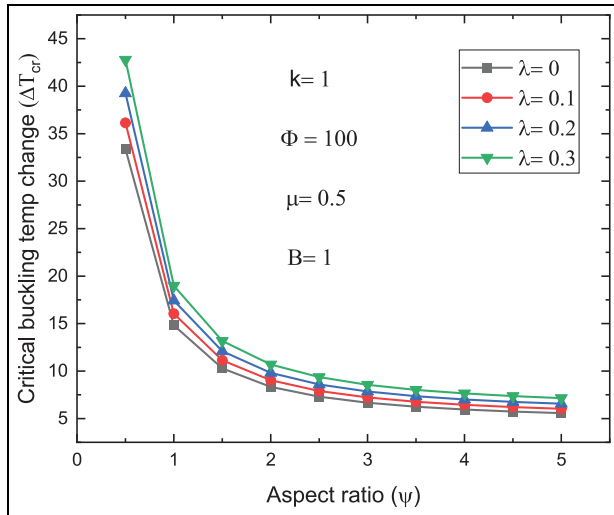


**Figure 19.** The critical buckling temperature change  $\Delta T_{cr}$  of simply-supported Al/SiC sinusoidal geometrical imperfect porous FGP under uniform temp rise versus aspect ratio  $\psi$  and porosity index  $\lambda$  ( $B = 1$ ).

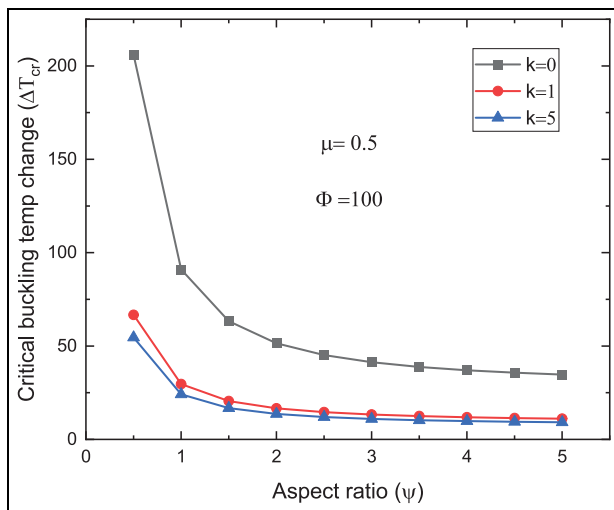


**Figure 20.** The critical buckling temperature change  $\Delta T_{cr}$  of simply-supported Al/SiC sinusoidal geometrical imperfect non-porous FGP under longitudinal temp changes versus aspect ratio  $\psi$  and power-law index  $k$ .

critical buckling temperature  $\Delta T_{cr}$  decreases as the volume fraction index increases.

In Figures 17 to 19, the critical buckling temperature  $\Delta T_{cr}$  of porous FGP (for  $k = 1$ ,  $\phi = 100$ , and  $\mu = 0.5$ ) under uniform temperature rise has been investigated. The effective materials properties of porous FGP have been computed using equation (1). It can be seen from the results that the critical buckling temp change  $\Delta T_{cr}$  increases with increasing the porosity volume fraction  $\lambda$  and decreasing the aspect ratio  $\psi$ . It is noteworthy that the influence of porosity on the critical buckling temperature change decreases as the aspect ratio increases.

It is also observed that the Critical buckling temperature change  $\Delta T_{cr}$  decreases as the porosity distribution changes form even ( $B = 0$ ) to uneven ( $B = 1$ ).

In Figure 20, the critical buckling temperature change  $\Delta T_{cr}$  of FGP when it is subjected to linear longitudinal temperature variation has been shown. The temperature variation has been given using equation (48). It is observed that the change in buckling temperature is almost double compared to the case of FGP under uniform temperature rise.

## Conclusion

In the current paper, equilibrium, stability, and compatibility equations for simply-supported geometrically imperfect porous functionally graded plates are derived. The derivation is based on the four variable refined plate theory with a von-Karman sense of geometric nonlinearity. The buckling response of FGP under several geometric configuration and loading conditions has been explored. It is concluded that:

- The buckling load of a perfect FGP is less than a geometrically imperfect plate.
- The critical buckling load of an FGP is proportional to imperfection amplitude  $\mu$ .
- The changes in an aspect ratio  $\psi$  of the plate lead to changes in the buckling mode of the plate considerably.
- The classical plate theory overestimates the buckling load whereas the third-order shear deformation theory and four variable refined plate theory deliver the result very close to each other for thick as well as thin plates.
- The critical buckling load  $\delta_{cr}$  for the FGPs increases with the decreases of aspect ratio  $\psi(a/b)$ .
- The critical buckling load  $\delta_{cr}$  for the FGP increases with decreases in the side to thickness ratio  $\phi$  or  $\Phi$ .
- The critical buckling load  $\delta_{cr}$  for the plates under biaxial compression is less than the plates under uniaxial compression.
- The critical buckling load  $\delta_{cr}$  for the plates under uniaxial and biaxial compression is less than for plates under combined tension and compression. This conclusion suggests that the addition of a tensile load in the transverse direction is seen to have a stabilizing effect.
- The critical buckling load  $\delta_{cr}$  for FGP decreases as the porosity volume fraction  $\lambda$  increase.
- Critical buckling load  $\delta_{cr}$  increases as the porosity distribution changes form even ( $B = 0$ ) to uneven ( $B = 1$ ).
- The critical buckling temp change  $\Delta T_{cr}$  of an FGP is proportional to imperfection amplitude  $\mu$ .
- The critical buckling temp change  $\Delta T_{cr}$  for the FGP increases with decreases in the side-to-thickness ratio  $\phi(a/h)$  or  $\Phi(b/h)$ .

- The critical buckling temp change  $\Delta T_{cr}$  for the FGP generally increases with decreases in the aspect ratio  $\psi$ .
- The plate under linear longitudinal temperature change  $\Delta T_{Lcr}$  is twice that of the plate subjected to uniform temperature change  $\Delta T_{ucr}$ .
- The Critical buckling temperature change  $\Delta T_{cr}$  for FGPs subjected to global imperfection is higher than for plates with sine-type imperfection.
- The critical buckling temp change  $\Delta T_{cr}$  for the FGP increases as the porosity volume fraction  $\lambda$  increase.
- The Critical buckling temperature change  $\Delta T_{cr}$  decreases as the porosity distribution changes form even ( $B = 0$ ) to uneven ( $B = 1$ ).


### Declaration of conflicting interests

The author(s) declared no potential conflicts of interest with respect to the research, authorship, and/or publication of this article.

### Funding

The author(s) received no financial support for the research, authorship, and/or publication of this article.

### ORCID iD

Ankit Gupta  <https://orcid.org/0000-0002-2961-225X>

### References

1. Koizumi M and Niino M. Overview of FGM research in Japan. *MRS Bull* 1995; 20: 19–21.
2. Gupta A and Talha M. Recent development in modeling and analysis of functionally graded materials and structures. *Prog Aerosp Sci* 2015; 79: 1–14.
3. Xu YP and Zhou D. Three-dimensional elasticity solution of simply supported functionally graded rectangular plates with internal elastic line supports. *J Strain Anal Eng Des* 2009; 44: 249–261.
4. Naj R, Boroujerdy MS and Eslami MR. Thermomechanical instability of functionally graded truncated conical shells with temperature-dependent material. *J Strain Anal Eng Des* 2008; 43: 259–273.
5. Boroujerdy MS and Eslami MR. Thermal buckling of piezoelectric functionally graded material deep spherical shells. *J Strain Anal Eng Des* 2013; 49: 51–62.
6. Shariat BAS, Javaheri R and Eslami MR. Buckling of imperfect functionally graded plates under in-plane compressive loading. *Thin Walled Struct* 2005; 43: 1020–1036.
7. Lanhe W. Thermal buckling of a simply supported moderately thick rectangular FGM plate. *Compos Struct* 2004; 64: 211–218.
8. Javaheri R and Eslami MR. Buckling of functionally graded plates under in-plane compressive loading. *ZAMM Zeitschrift für Angew Math und Mech* 2002; 82: 277–283.
9. Gupta A and Talha M. Influence of porosity on the flexural and free vibration responses of functionally graded plates in thermal environment. *Int J Struct Stab Dyn*. Epub ahead of print January 2018. DOI: 10.1142/S021945541850013X.
10. Gupta A and Talha M. Influence of initial geometric imperfections and porosity on the stability of functionally graded material plates. *Mech Based Des Struct Mach* 2018; 46: 693–711.
11. Mohammadi M, Saidi AR and Jomehzadeh E. A novel analytical approach for the buckling analysis of moderately thick functionally graded rectangular plates with two simply-supported opposite edges. *Proc IMechE, Part C: J Mechanical Engineering Science* 2010; 224: 1831–1841.
12. Zhang J, Pan S and Chen L. Dynamic thermal buckling and postbuckling of clamped–clamped imperfect functionally graded annular plates. *Nonlinear Dyn* 2019; 95: 565–577.
13. Fazzolari FA, Banerjee JR and Boscolo M. Buckling of composite plate assemblies using higher order shear deformation theory—an exact method of solution. *Thin Walled Struct* 2013; 71: 18–34.
14. Thai HT and Choi DH. An efficient and simple refined theory for buckling analysis of functionally graded plates. *Appl Math Model* 2012; 36: 1008–1022.
15. Shariat BAS and Eslami MR. Thermomechanical stability of imperfect functionally graded plates based on the third-order theory. *AIAA J* 2006; 44: 2929–2936.
16. Shariat BAS and Eslami MR. Buckling of thick functionally graded plates under mechanical and thermal loads. *Compos Struct* 2007; 78: 433–439.
17. Gupta A and Talha M. Influence of micro-structural defects on post-buckling and large-amplitude vibration of geometrically imperfect gradient plate. *Nonlinear Dyn* 2018; 94: 39–56.
18. Shariat BAS and Eslami MR. Buckling of functionally graded plates under in plane compressive loading based on the first order plate theory. In: *Proceeding of the Fifth international conference on composite science and technology*. Sharjah, UAE: American University of Sharjah, 2005.
19. Mojahedin A, Jabbari M, Khorshidvand AR, et al. Buckling analysis of functionally graded circular plates made of saturated porous materials based on higher order shear deformation theory. *Thin Walled Struct* 2016; 99: 83–90.
20. Bouiadjra MB, Ahmed Houari MS and Tounsi A. Thermal buckling of functionally graded plates according to a four-variable refined plate theory. *J Therm Stress* 2012; 35: 677–694.
21. Alijani F and Amabili M. Non-linear dynamic instability of functionally graded plates in thermal environments. *Int J Non Linear Mech* 2013; 50: 109–126.
22. Yanga J and Shen HS. Non-linear analysis of functionally graded plates under transverse and in-plane loads. *Int J Non Linear Mech* 2003; 38: 467–482.
23. Dinh N and Van Tung H. Mechanical and thermal post-buckling of higher order shear deformable functionally graded plates on elastic foundations. *Compos Struct* 2011; 93: 2874–2881.
24. Li SR, Zhang JH and Zhao YG. Nonlinear thermomechanical post-buckling of circular FGM plate with geometric imperfection. *Thin Walled Struct* 2007; 45: 528–536.
25. Shariat BAS and Eslami MR. Thermal buckling of imperfect functionally graded plates. *Int J Solids Struct* 2006; 43: 4082–4096.



26. Shariat BAS and Eslami MR. Effect of initial imperfections on thermal buckling of functionally graded plates. *J Therm Stress* 2005; 28: 1183–1198.
27. Liew KM, Yang J and Kitipornchai S. Postbuckling of piezoelectric FGM plates subject to thermo-electro-mechanical loading. *Int J Solids Struct* 2003; 40: 3869–3892.
28. Sherafat MH, Ovesy HR and Ghannadpour SAM. Buckling analysis of functionally graded plates under mechanical loading using higher order functionally graded strip. *Int J Struct Stab Dyn* 2013; 13: 1–13.
29. Morimoto T and Tanigawa Y. Linear buckling analysis of orthotropic inhomogeneous rectangular plates under uniform in-plane compression. *Acta Mech* 2006; 187: 219–229.
30. Abrate S. Free vibration, buckling, and static deflections of functionally graded plates. *Compos Sci Technol* 2006; 66: 2383–2394.
31. Bodaghi M and Saidi AR. Levy-type solution for buckling analysis of thick functionally graded rectangular plates based on the higher-order shear deformation plate theory. *Appl Math Model* 2010; 34: 3659–3673.
32. Park JS and Kim JH. Thermal postbuckling and vibration analyses of functionally graded plates. *J Sound Vib* 2006; 289: 77–93.
33. Uymaz B and Aydogdu M. Three dimensional mechanical buckling of FG plates with general boundary conditions. *Compos Struct* 2013; 96: 174–193.
34. Suganyadevi S and Singh BN. Higher-order closed-form solution for the analysis of laminated composite and sandwich plates based on new shear deformation theories. *Compos Struct* 2013; 75: 324–336.
35. Shahverdi H and Barati MR. Vibration analysis of porous functionally graded nanoplates. *Int J Eng Sci* 2017; 120: 82–99.

## Appendix I

### Notation

$a$	the length of plate
$b$	the width of plate
$h$	the thickness of plate
$K$	power law index
$\alpha_T$	coefficient of thermal expansion
$u, v, w$	mid-plane displacement
$u_0, v_0, w_0$	initial displacement
$f(z)$	shear strain function
$\psi(a/b)$	aspect ratio
$\delta_{cr}$	critical buckling load
$E_c$	Young modulus of ceramic
$E_m$	Young modulus of metal
$\sigma_{ij}$	stress
$\varepsilon_{ij}$	strain
$\gamma$	load ratio
$\mu$	imperfection amplitude
$\phi(a/h)$	side-to-thickness ratio
$\lambda$	porosity volume fraction
$\Phi(b/h)$	side-to-thickness ratio
$\Delta T_{cr}$	critical buckling temperature difference